Analysis of middle-to-far wake behind floating offshore wind turbines in the presence of multiple platform motions

Alireza Arabgolarcheh [a,*], Amirhossein Rouhollahi [a,b], Ernesto Benini [a]

[a] *Department of Industrial Engineering, University of Padova, Via Venezia 1, 35131, Padova, Italy*
[b] *Department of Aerospace Engineering, Amirkabir University of Technology (Tehran Polytechnic), Tehran, Iran*

ARTICLE INFO

ABSTRACT

Understanding the unsteady characteristics of the mid-to-far wake and comprehension of the aerodynamic performance of floating offshore wind turbines is essential for the further development of offshore wind farms. In this perspective, a developed Actuator line model is utilized to analyze an offshore turbine on four different platforms. The model reliability was examined through three sets of validations involving turbine output in fixed and floating conditions and wake expansion in terms of size and rate. The affected relative velocity by the platform motion contributes to the wake deformation and temporal effects on induced velocity. Angular platform motions produce a non-axisymmetric helical wake that raises the chance of meandering wake patterns. It was founded although platform movement generally can boost the recovery of mean velocity value, it may amplify the amplitude of velocity deficit fluctuation at further downstream by encouraging interactions and merging vortex rings. Consequently, the wake propagates into a form of stronger circles whose period, strength, and center are functions of turbine movement and operation conditions. By providing a computationally efficient tool, the findings emphasize the importance of wake propagation in designing and assessing farm layouts that operate in the presence of significant multi-motions of floating offshore wind turbines.

1. Introduction

Wind energy plays a significant role in the global transition toward sustainable green energy, and its demand has remarkably increased in recent years [1]. In the wind energy sector, offshore wind energy has risen rapidly, expecting the 35 GW capacity in 2022 to grow above 380 GW by 2030 and 2000 GW by 2050 [2]. Floating offshore wind turbines (FOWTs) are of particular interest, as they goes ahead of the fixed turbines in shallow waters and exploits the higher potential of wind energy in deep waters by employing floating platform systems [3].

During the past decade, a particular demand for the unsteady aerodynamics of FOWTs has been drawn [4]. A critical challenge in developing FOWTs is the complex aerodynamics of a moving rotor, which poses challenges to the farm design, structural design, and control [5–8]. Complex rotor motions and the subsequent local aerodynamics have become more prevalent, but they are still not as developed as fixed rotor aerodynamics [4]. The effects of platform motion in wind farm design is an area that needs to be understood more. The available numerical methods for study of wind turbine aerodynamics have their own cons and pros when it comes to floating wind turbine wake. High-fidelity studies like CFD have rarely been utilized for the hydro-aerodynamic simulation of FOWTs [9]. Although they provide practical data, their computational cost is a drawback.

The Blade Element Momentum model (BEM) is one of the most common models for the aerodynamic simulation of wind turbines [10]. The OpenFAST [11] code, developed by NREL, is a BEM-based code equipped with generalized dynamic wake (GDW) theory. Many researchers use this solver for onshore and floating wind turbine design [12]. Jonkman and Matha [13] have employed it for dynamic-response analysis of FOWT platforms, Sebastian and Lackner [14] used it to study the wake behind a FOWT, and Li et al. [15] utilized this solver to investigate the yawed-inflow effect on platform motions and dynamic characteristics of the FOWT. The main advantages of the BEM model are its incomparable low computational cost and availability of open-source codes. One important inherent inadequacy is its weaknesses in modeling 3D flow across radial elements, which limits the accuracy of the simulation, especially in unsteady 3D motions such as pitch [4,16,17].

Free Vortex Methods (FVMs) are relatively new methods that proved to produce reliable results for wind turbine aerodynamic output [18]. FVM offers a more sophisticated model for simulating FOWT aerodynamics than BEM, as it uses vortex filaments to model the wake. Shen

---

* Corresponding author.

E-mail address: alireza.arabgolarcheh@phd.unipd.it (A. Arabgolarcheh).

Nomenclature

A_d	Linear amplitude [m]
A_θ	Angular amplitude [rad]
B	Number of blades [−]
C_P	Power coefficient [−]
C_l, C_d, C_m	Lift, drag and moment coefficient [−]
C_1	Model coefficient [s]
C_2	Model coefficient [−]
c	Chord Length [m]
d	Linear displacement [m]
f	Frequency of oscillation [Hz]
$F_{turbine}$	The body force that represents the whole turbine
F_l, F_d	Lift and drag force [N]
g	Gravity acceleration [ms^{-2}]
M	Pitching moment [Nm]
p	Pressure [Pa]
r	Distance from actuator point to the point where the force is applied [m]
R	Blade radius [m]
t	Time [s]
u	Flow velocity [ms^{-1}]
$\vec{U}_{rel}$	Relative velocity [ms^{-1}]
$\vec{U}_{inflow}$	Inflow velocity [ms^{-1}]
$\vec{U}_{rotor\ rotation}$	Velocity of the element due to rotor rotation [ms^{-1}]
$\vec{U}_{platform}$	Velocity of the element due to platform motion [ms^{-1}]
V_{cell}	Volume of the cell [m^3]
w	Section width [m]

Greek letters

α	Local angle of attack [rad]
β	Pitch angle [rad]
ρ	The density of the fluid [kgm^{-3}]
ε	Projection width [m]
ε	Turbulent kinetic energy dissipation rate [m^{2}s^{-3}]
θ	Angular displacement [rad]
λ	Tip speed ratio [−]

Acronym

ADM	Actuator Disk Model
ALM	Actuator Line Model
BEM	Blade Element Momentum
DOF	Degrees Of Freedom
FAST	The Fatigue, Aerodynamics, Structures, and Turbulence program
FOWT	Floating Offshore Wind Turbine
FVM	Free Vortex Method

et al. used FVM to study surging [19] and pitching [20] motions in FOWTs, while Rodriguez and Jaworski [21,22] used this model in aeroelastic coupling for FOWTs. Although this inviscid model is based on potential flow and requires corrections factors for each test case, the fidelity of the FVM method is still higher than BEM [23], particularly in wake prediction.

In the Actuator Disc Model (ADM), the actuator disk theory is coupled with the CFD resolved flow field that provides a higher fidelity compared to BEM with a computational cost less than blade-resolved CFD simulations [24]. De Vaal et al. [25], Micallef and Sant [26], and Kopperstad et al. [27] utilized CFD-AD to analyze FOWT in surge motion, and Rezaeiha and Micallef [28] used it to study floating turbine-to-turbine interaction while the first turbine is surging and the second turbine is steady. The limit of this method is in modeling wake swirl, which makes it unable to capture realistic helical geometry of wake [29]. Moreover, due to the circumferentially averaged data for rings, this method cannot address angular platform motion and other phenomena that depend on the azimuth angle. Actuator Line Method (ALM) is a leading hybrid method that rotates a line of momentum sources in lieu of each blade. Considering the rotation of the blades makes the approach capable of modeling wake swirl [30,31] and angular platform motion that provide higher fidelity than BEM and CFD-AD [32–34] with still less computational cost than the blade-resolved CFD [35].

In wind farm design, the axial velocity distribution behind a rotor affects the inflow that the downstream wind turbines receive. This inflow condition plays the main role in estimating the aerodynamic and fatigue loads on the downstream floating wind turbine [28,36–38]. Medium-fidelity approaches, particularly CFD-AD, were dominantly limited to the study of surge motion [27,28] due to their inherent weakness in simulating skewed flows.

A few researchers have employed ALM for the aerodynamic simulation of FOWTs. Corniglion et al. [34] compared the results of ALM with FVM for NREL 5 MW turbine and investigated just the surge motion in rated operating conditions while focusing on the near-wake flow. Apsley et al. [32] utilized ALM and compared it to BEM in the NREL 5 MW turbine simulation with a prescribed sinusoidal wind speed fluctuation in different operating conditions instead of considering platform motions. Johlas et al. [39] performed an LES simulation coupled with ALM to study the wake of the NREL 5 MW turbine. They performed a 6-DOF simulation for two different floating platforms at just below-rated conditions. Cheng et al. [40,41] developed a coupled aero-hydrodynamic model to simulate the NREL 5 MW turbine in six-DOF motion at the rated conditions. In all of these ALM simulations, the rotor aerodynamics was the primary emphasis, leaving the downstream wake, particularly the mid-to-far wake, unstudied.

As reported, while there are a few studies regarding the wake behavior behind offshore wind turbines in floating conditions, the applications of AL models were mainly limited to the study of a single degree of motion. To the best of the authors' knowledge, the ALM study of FOWTs with realistic multi motions under different operation conditions still remains uninvestigated. The main aim of this paper is to develop an AL model to study the effects of the platform motions on its aerodynamic performance and wake evolution at different operating conditions. Analyzing the velocity deficit behind different platforms with multi degrees of motion at different operation and environmental conditions reveals their effects on wake recovery.

The paper is organized as follows. The numerical modeling method and the theory of the modified ALM for floating motions are described in Section 2. In section 3, after describing the numerical model, the validity of the results is investigated. The test matrices, which include the platforms and operational characteristics and describe the details of platform motions, is presented in section 4. Then in section 5, the wind turbine aerodynamic and wake analysis under multi-DoF motions are presented. Finally, conclusions are drawn in Section 6.

2. Numerical method

In this study, a supplementary C++ library for AL modeling in floating conditions is developed and coupled with the OpenFOAM toolbox. In this way, the flow field, turbulence model, and other potential equations are solved by the OpenFOAM, and the implemented ALM library determines the actuator lines.

2.1. CFD computational settings

The turbulent flow field around the wind turbine was computed by the finite volume method (FVM). The three-dimensional unsteady Reynolds-averaged Navier–Stokes equations (URANS) were employed. The Realizable $k - \varepsilon$ turbulence model was used for its relatively low computational cost associated with the computation of the turbulent viscosity. Regarding the temporal discretization, a second-order Crank–Nicolson method was applied for time integration. The PIMPLE algorithm was adopted for pressure-velocity coupling, a combination of SIMPLE and PISO algorithms. The matrices are solved by choosing the generalized geometric-algebraic multigrid (GAMG) for pressure and a preconditioned bi-conjugated gradient (PBiCG) for velocity [42].

2.2. Actuator line model

The fundamental philosophy behind the actuator line methodology is to substitute the physical geometry of the blades with only its impact on the flow field. The ALM uses a chain of spanwise element points in place of sections, each with a constant airfoil, twist, chord, and oncoming wind. The volumetric forces made by each blade section are projected into the flow field, whereby it inserts the same forces on the fluid as the turbine blades through source terms in the momentum equations.

The developed ALM code initially calculates the relative velocity based on the following equation:

$$\overrightarrow{U}_{rel} = \overrightarrow{U}_{inflow} + \overrightarrow{U}_{rotor\ rotation} + \overrightarrow{U}_{platform} \tag{1}$$

where $\overrightarrow{U}_{rel}$ indicates the relative velocity resulting from inflow velocity, the rotor's rotation, and the platform's motion. The inflow velocity is calculated using an average sampling approach. Next, the local angle of attack, defined as the angle between the chord and the local flow, is calculated based on equation (2), where $\hat{n}$ is the unit normal vector of the planform.

$$\alpha = \sin^{-1} \left(\left(\overrightarrow{U}_{rel}.\hat{n} \right) \Big/ \left| \overrightarrow{U}_{rel} \right| \right) \tag{2}$$

The aerodynamic forces of the blade sections are calculated based on the lift and drag coefficients obtained from the airfoil database, as follows:

$$F_l = \frac{1}{2} C_l(\alpha) \rho \left| \overrightarrow{U}_{rel} \right|^2 cw \hat{e}_l \tag{3}$$

$$F_d = \frac{1}{2} C_d(\alpha) \rho \left| \overrightarrow{U}_{rel} \right|^2 cw \hat{e}_d \tag{4}$$

here C_l and C_d are lift and drag coefficients, c is chord length, w is section width, and $\hat{e}_l$ and $\hat{e}_d$ are unit vectors in directions of lift and drag, respectively.

To consider the tip effect and the rotational effects, a tip function is defined as follows [43]:

$$f_{tip} = \frac{2}{\pi} arccos \left[exp \left(-g \frac{B(R-r)}{2\ r\ sin(\alpha+\beta)} \right) \right] \tag{5}$$

here β is the pitch angle that includes blade pitch and twist. The g coefficient depends on different parameters such as the number of blades, TSR (λ), and chord distribution. For simplicity, the function is chosen to be only dependent on the variable $B\lambda$ as follows:

$$g = exp[-C_1(B\lambda - C_2)] + 0.1 \tag{6}$$

Coefficients C_1 and C_2 were determined empirically using data at two different tip speed ratios (NREL rotor at 10 m/s and WG 500 rotor at TSR = 14) [44]. The function is shifted with a minor value of 0.1 to be

consistent for infinite tip speed ratio cases or an infinite number of blades. The final form uses C_1 and C_2 whose values are 0.125 and 21, respectively. Function g is needed to adjust the influence of the tip vortices on pressure distribution in the blade tip region [43]. Although Shen's tip correction is not an ideal physical model for ALM application, it relived a promising result for ALM applications according to the references [43,45–50].

To avoid numerical instability and provide a smooth force projection, these forces are projected into the flow field by applying a 3D isotropic Gaussian function as follows [51]:

$$\boldsymbol{F}_{field}(x_c, y_c, z_c, t) = -\sum_N \sum_e \overrightarrow{F}_{N,e}(x_{N,e}, y_{N,e}, z_{N,e}, t) f_{tip} \eta_{N,e} \tag{7}$$

$$\eta = \frac{1}{\varepsilon^3 \pi^{3/2}} \exp \left[-\left(r \big/ \varepsilon \right)^2 \right] \tag{8}$$

where $\boldsymbol{F}_{field}$ is the volumetric force field at the position of the cells, and $\overrightarrow{F}$ indicates the forces at actuator element points calculated based on lift and drag forces. Also, N is the body index (i.e., blades, hub, and tower), and e denotes the actuator element point index. The parameter η represents the Gaussian function, r is the distance between the actuator point and the grid cell center, and ε is the projection width, which is the maximum value among the chord factor, drag factor, and mesh factor, as the following:

$$\varepsilon = \max \left[\frac{c}{4}, \frac{cC_d}{2}, 4\sqrt[3]{V_{cell}} \right] \tag{9}$$

In the developed ALM code, the linear and angular velocity vector can be determined using either a prescribed movement or the acting forces and moments on the turbine. For more detail about the current developed code, readers are referred to a previous paper by the current authors [29].

3. Code verification and validation

3.1. Wind turbine model

The NREL 5-MW wind turbine was designed by the National Renewable Energy Laboratory to be a representative utility-scale wind turbine suitable for a floating offshore installation. This turbine is a popular reference case as it is studied in different researches including, aerodynamic, structure [4], and control [52,53]. This is a conventional three-blade upwind turbine with a rotor diameter of about 126 m and a hub height of nearly 90 m. The blades are composed of a series of Delft University (DU) and NACA 64xxx airfoils, as shown in Fig. 1. The turbine properties are presented in Table 1. This turbine is designed as a variable-speed variable-blade-pitch-to-feather-controlled turbine. The rated wind speed is 11.4 m/s, and in the rated wind speed, the rotor speed is 12.1 rpm, and the produced power is 5 MW.

A cuboid computational domain in a Cartesian coordinate system was used in this study that consists of non-conformal hexahedral (cubic) grids, as shown in Fig. 2. This type of mesh makes local refinement possible in the areas of interest that can significantly reduce the
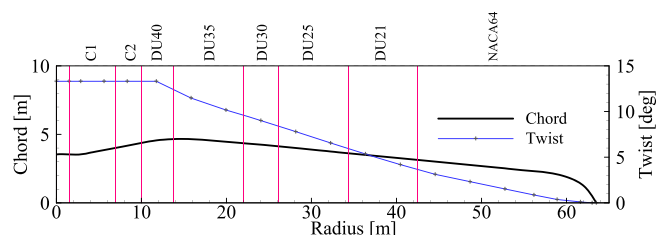

Fig. 1. NREL 5 MW Chord and twist design.

Table 1
Properties of NREL 5 MW wind turbine.

Parameter	Value	Parameter	Value
Rotor configuration	Upwind	Power Output	5 MW
Number of blades	3	Cut-in wind speed	3 m/s
Rotor diameter	126 [m]	Rated wind speed	11.4 m/s
Hub height	90 [m]	Cut out wind speed	25 m/s
Rotor Mass	53220 kg	Rated Tip Speed	80 m/s
Air density	1.23 [kg/m^3]	Cut-in rotor speed	6.9 rpm
Air kinematic viscosity	1.46e-5 [m^2/s]	Rated rotor speed	12.1 rpm
Blade sectional profiles	DU and NACA series	Overhang—Shaft Tilt—Precone	5m—5°–2.5°

computational resources required for the simulation. The boundary conditions for the wind turbine simulation are expressed in Fig. 2-a. A uniform freestream velocity was applied for the inlet boundary condition. The inlet velocity magnitude was set to the examined conditions, and the direction was set in the X-direction. A pressure outlet boundary condition was set for the outlet condition, and the reference pressure was selected the standard atmospheric pressure. Consequently, the dynamic pressure field is determined considering this condition. The no-slip boundary conditions were applied for the two lateral walls, the base and the upper side of the domain.

3.2. Verification

The verification examinations methodology for domain size, mesh resolution, and time step size are described in more detail in ref. [29]. The same procedure was accomplished for mesh and time step size verification. Accordingly, the coarsest cell size in region one was determined as 10.5 [m]. As the refined regions are shown in Fig. 2, region 4 was expanded in wind direction and opposite to cover the most extended motion. A time step size of 1° was also determined based on a verification study. Prior to any data sampling, the number of time steps necessary for a converged solution was revealed. The time history of the power coefficient (C_P) and power coefficient change relative to the last

rotor revolution ($\Delta C_P / C_{P,30}$) showed following 20 revolutions, the difference between two consecutive revolutions was less than 0.2% and the value of ΔC_P declined below 1%. This duration is adequate for the validation of the turbine output. The development of the wake takes a longer time. Therefore, to avoid omitting unsteady phenomena in the floating conditions, the results are reported for a longer duration of time.

The height and width of the selected domain were set to 4D and 6D. Due to the chosen outlet boundary condition and inlet boundary condition, the impact of upwind and downwind distances (d_i, d_o) on the produced power of wind turbine was investigated as described in Table 2. Accordingly, a cuboid of $15 \times 6 \times 4$ D was used as the computational domain to simulate the NREL 5 MW wind turbine.

3.3. Validations

Three sets of validation studies have been performed for the ALM code. In the first validation (see Fig. 3), the capability of the current ALM code in the simulation of the wind turbines was assessed. Since adequate experimental data are not available for this large-size wind turbine, the results were compared with other available high fidelity and low fidelity numerical models. The validation of the current code against experimental data of the NREL Phase VI was reported in a previous work by the authors [29]. In Fig. 3, the output power and rotor thrust of the

Table 2
Test matrix for the sensitivity study of the domain size.

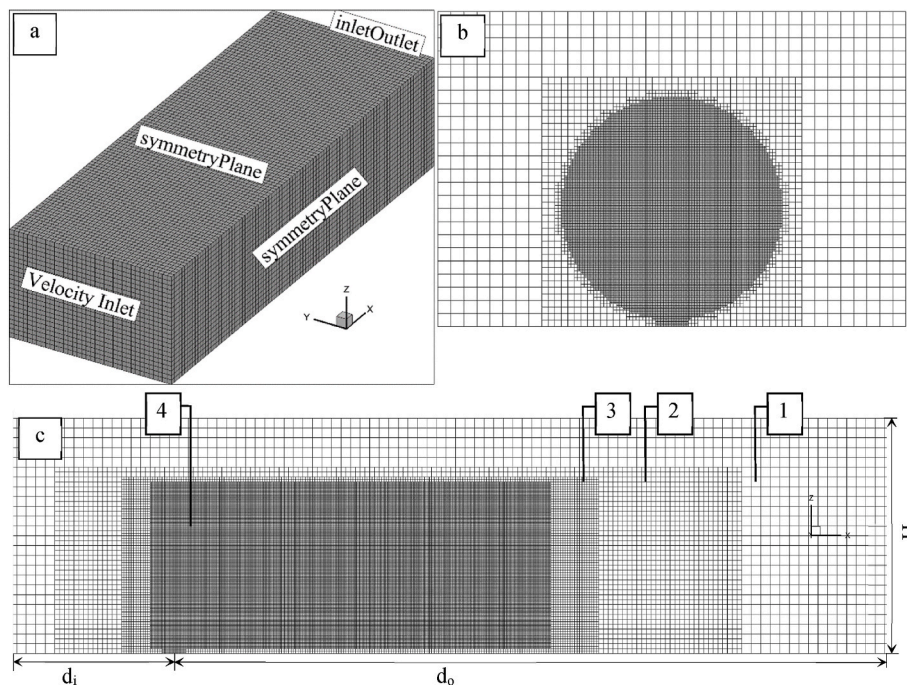| Case #	Distance to the inlet d_i/D	Distance to the outlet d_o/D	Domain Size $W \times H \times L$	# Cells	C_P/C_{P-ref}
1	1.5	12.5	336	981 k	1.1360
2	2.5	12.5	360	994 k	1.0025
3	4.5	12.5	408	1016 k	1.0022
4	8.5	12.5	504	1061 k	1.0017
5	2.5	5	180	966 k	1.0242
6	2.5	9	276	1011 k	1.0036
7	8.5	20	684	1078 k	1.0000

Fig. 2. (a) A schematic view for the computational domain and boundary conditions. (b) The computational grid from the front view, the section is on the rotor. (c) The computational grid from the side view, the section is on the tower axis.
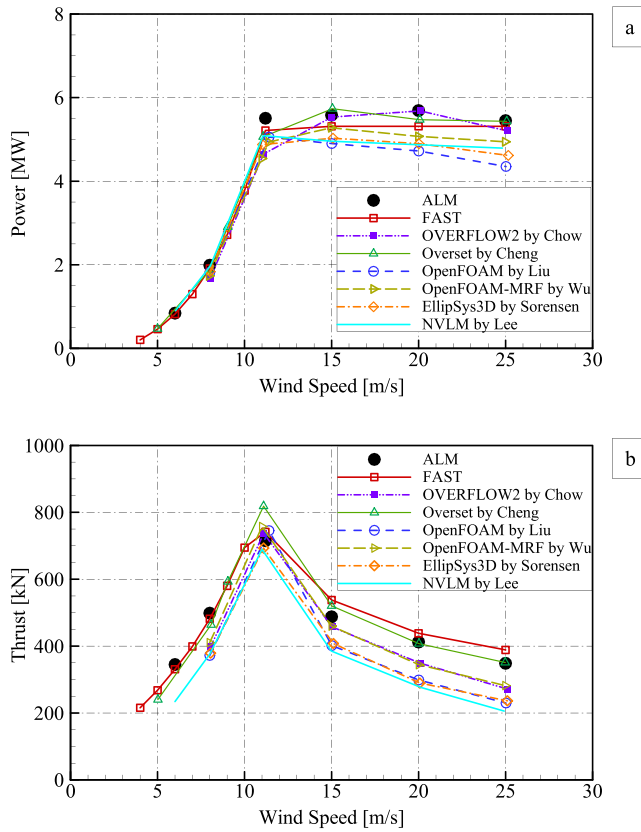
Fig. 3. Comparison of ALM results with the FAST code and other literature [40, 55,58–60] for NREL 5-MW wind turbine [29].

Fig. 4. Comparison of blade aerodynamic performance under surge motions [56,61].

fixed-bottom NREL 5 MW wind turbine were compared with BEM results obtained using the FAST code from NREL [54], OVERFLOW2 by Chow et al. [55], Overset by Cheng et al. [40], aeroelastic blade resolved CFD using OpenFOAM by Liu et al. [56], OpenFOAM-MRF by Wu et al. [57], EllipSys3D by Sorensen et al. [58] and the nonlinear vortex lattice method (NVLM) by Lee et al. [59]. Design and simulation parameters were chosen as similar as possible. Evaluating the rotor thrust showed a good general agreement with the blade resolved CFD simulations; likewise, the computed power output was consistent with the other data at the tested wind speeds. As it can be seen, the results of the ALM code are within the range of accuracy shown by blade resolved CFD models.

In the second validation study, the results of the current ALM code in a floating condition were compared with the other available in the open literature. Fig. 4 shows how the aerodynamic performance of the NREL 5 MW at a wind speed of 11.4 [m/s] and rotor speed of 12.1 [RPM] changes under a prescribed platform surge motion with an amplitude of 2 [m] and a period of 12 [s]. The current ALM code results are compared with FAST v8 and CFD by Liu et al. [56] and CFD for a rigid and flexible turbine by Wu et al. [61]. To obtain the ALM result presented in Fig. 4, the design and simulation parameters were chosen as much similar as possible to Liu et al. [56] and Wu et al. [61]. The tower, nacelle, and hub are ignored, and the shaft tilt angle was set to zero.

The variation of thrust and power were in the order of 10% and 20%, respectively. As it can be seen, the trends are well reproduced, and the values are relatively close. Generally, a slightly larger turbine aerodynamic output is predicted by the ALM and FAST codes. While the ALM and FAST use some empirical correction, the mesh used by the mentioned CFD projects does not appear to be fine enough for capturing all airfoil vortices. In overall, although all of the mentioned methods have their limitations, the results are quite close [56].

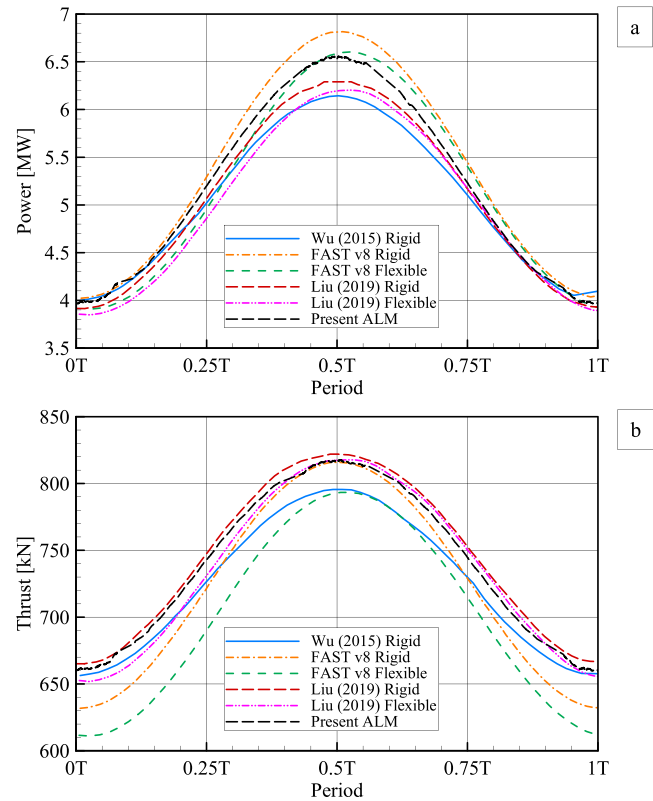The third section of validation aims to investigate the wake

simulation accuracy of ALM by comparing its results with both higher and lower fidelity approaches. In this regard, the results for the NREL Phase VI case [29] were compared to the semiempirical models (i.e., Jensen, Larsen, and Frandsen models) and LES simulation by Sedaghatizadeh et al. [62]. The wake expansion is presented in Fig. 5-a, where the wake diameter is calculated based on the highest velocity gradient to make a quantitative comparison [62]. This diameter could be an appropriate representation of the boundary between the low-velocity region in the wake and the free stream. A uniform incoming velocity profile in a free environment was used for this plot to make a similar environment.

As Fig. 5-a demonstrates, semiempirical engineering models overestimate the wake expansion rate and the wake diameter. Despite the simplicity of the method, ALM predicts the near-wake expansion ($x < 4D$) with approximately the same wake diameter calculated by LES. The near wake refers to the area where the wake converses its helical shape. Even in the mid to far wake region ($4D < x < 7D$), where the break-down of tip vortices takes place, and the gradients are still high, the difference with LES is still insignificant. The LES results show that the wake dimeter starts to decrease after 9D. This phenomenon can only be captured by ALM and LES models since they consider the mixing of the wake with the ambient flow when resolving the flow field.

Few discrepancies between ALM and LES are visible in the far wake region. While the results are fairly similar in the near wake, this difference is addressed by the different turbulence models. The turbulent mixing plays a key role in wake break-down. The URANS models overestimate turbulence, leading to a faster turbulent momentum diffusivity and a quicker wake recovery. LES models predict a later decay of the wake and a more precise wake interference, as reported in ref. [63].

It should be noted that the computational time of ALM code for this case was just 1.37% of the LES model. In addition, due to the sensitivity of the LES model to input data, an accurate LES model might require
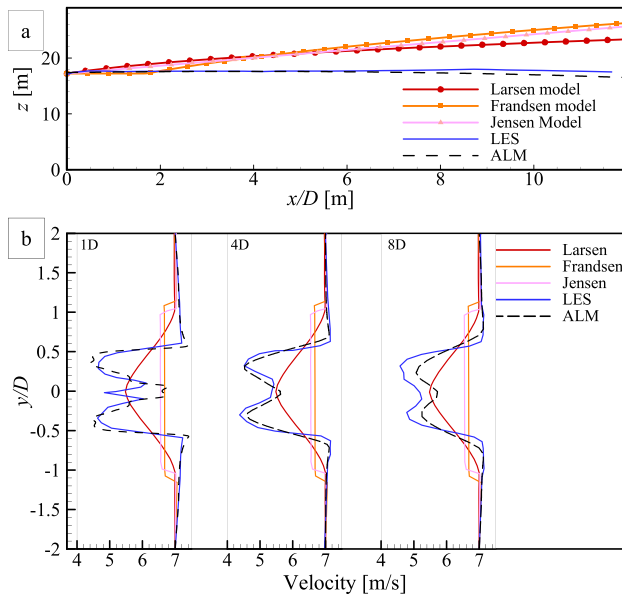
Fig. 5. Wake behind the NREL Phase VI, a) The expansion of wake diameter calculated by different models b) Comparison of velocity profiles on the horizontal plane passing through the hub height at different streamwise locations by the current ALM and ref. [62].

input data that make measurements necessary. Despite a considerable difference in computational cost, the difference in the results might be negligible as the slope of decreasing the wake diameter at 9D downstream was −0.198 versus 0.102, calculated respectively by the current ALM-URANS and LES.

The calculated velocity profiles downstream of the wind turbine are plotted in Fig. 5-b. Comparing the profiles indicates that while the deviation of semiempirical models from LES is intense behind the wind turbine, ALM is in agreement with LES. The velocity profiles in Fig. 5-b indicate that the amplification deviation by semiempirical models from LES is even more intense, while ALM is still in agreement with LES. ALM produces a more accurate velocity profile inside the wake region (see Fig. 5-b). Despite the simplicity of the ALM, it provided satisfactory wake diameters and velocity profiles in the near wake (up to 4D). Further downstream, the ALM deviates from the LES by underestimating wake influence and velocity deficit. This difference can be due to the overestimation of recovery rates by standard URANS models [63]. It is important to note that the velocity profile produced using the semi-empirical models is axisymmetric. The ALM, similar to the LES, captures a slightly non-axisymmetric profile as a result of blade rotations. This is another plus of the ALM, as unlike the actuator disk model considers the blades separately and without averaging circumferentially.

3.4. Test matrix

The current study is focused on the aerodynamic effects caused by floating platform motions regardless of the mechanisms generating the motions. The impact of multiple-DoF motions on the aerodynamic load and wake structure is studied in the next section. Three well-known platforms were selected to study the NREL 5 MW wind turbine. The OC3-Hywind spar buoy platform proposed by the Offshore Code Comparison Collaboration (OC3) project (IEA) [64], the MIT/NREL TLP platform developed by the Massachusetts Institute of Technology (MIT) [65], and the ITI Energy barge platform developed by the Universities of Glasgow and Strathclyde [66]. These configurations have been selected since they are three well-known and well-documented floating platform models that were studied in several aerodynamic-hydrodynamic

analyses. The physical properties of the mentioned platform models are summarized in Table 3.

Sebastian and Lackner [14] proposed a power spectral density (PSD) approach that was followed by other researchers, including Lee and Dong [67,68]. They utilized a power spectral density (PSD) analysis to determine the main platform DoF contributing to inflow velocity variation and angle of attack. In this way, only primary platform modes are imposed rather than applying the actual time series of platform motions produced by hydrodynamic codes. Classifying the aerodynamic contribution of a platform motion mode from other modes is complicated in the presence of many platform modes that reveal similar spectral peaks. Sebastian and Lackner [14] showed that most of the energy in each mode is attributed to two peak frequencies associated with the 1P rotor rate and the sea state. They modeled the actual time series using a linear superposition of two sinusoidal functions as follow:

$$X = X_0 + A_1 \sin(2\pi f_1 t + \varphi_1) + A_2 \sin(2\pi f_2 t + \varphi_2) \tag{10}$$

Table 4 lists a set of synthesized parameters that were fitted to the FAST-simulated responses of each platform under the mentioned operating conditions. Utilizing this approach, besides making it possible to analyze the aerodynamic effects of motion, provides a structure for cross-code comparison [67,68].

The operating and environmental conditions in this table are as follow.

1. Below-rated: $U_\infty = 6.0$ [m/s], $\lambda = 9.63$, $H_S = 1.83$ [m], $T_p = 12.72$ [s];
2. Rated: $U_\infty = 11.4$ [m/s], $\lambda = 7.00$, $H_S = 2.54$ [m], $T_p = 13.35$ [s];
3. Above-rated: $U_\infty = 18.0$ [m/s], $\lambda = 4.43$, $H_S = 4.09$ [m], $T_p = 15.33$ [s], $\theta_p = 15$ [°]

4. Results and discussion

This section presents the results of the NREL 5 MW wind turbine for platforms, operation, and environmental conditions stated in the test matrix section. Initially, the differences between operation conditions are introduced. Since the available literature for comparison is limited to the below-rated condition, the results of the below-rated condition are first analyzed and compared with other mid-fidelity approaches. After clarifying the effect of platform motion on the wake and rotor output, the paper focuses on the downstream velocity field in the three operation and environmental conditions and analyses the differences between velocity deficit affected by each platform motion.

Fig. 6 compares the side view of the visualized wake for the monopile platform under the three operating conditions. The wake visualization was performed using the iso-surface of Q-criterion equal to 0.001 and 0.0001, colored by velocity gradient magnitude. The helical geometries of the wakes are distinctly captured in all the three conditions and their

Table 3
Description of properties for the three floating platforms.

	OC3/Hywind spar-buoy	ITI energy barge	MIT/NREL TLP
Diameter or width × length [m]	6.5 to 9.5	45.14 (40 × 40)	18
Draft [m]	120	4	47.89
Water depth [m]	320	250	200
Displaced volume of water [m³]	8029.21	6000.0	12179.6
Mass [10³ kg]	7466.33	5452	8600.41
CM location below SWL [m]	89.92	0.28	40.61
Roll moment of inertia about CM [10⁶ kg-m³]	4229.23	726.9	571.624
Pitch moment of inertia about CM [10⁶ kg-m³]	4229.23	726.9	571.624
Yaw moment of inertia about CM [10⁶ kg-m³]	164.23	1453.9	361.408

Table 4

Platform motion parameters for the NREL 5 MW turbine with different floater types at three operating conditions.

| Operating conditions.	Floating platform	Mode	X_0 [m or °]	A_1 [m or °]	f_1 [Hz]	φ_1 [rad]	A_2 [m or °]	f_2 [Hz]	φ_2 [rad]
1	ITI Energy barge	Heave	−0.130	0.318	0.078	1.303	0.254	0.108	2.702
		Surge	13.602	0.725	0.007	−1.163	−0.442	0.078	2.609
		Pitch	0.591	1.475	0.078	−0.066	1.630	0.083	1.816
	OC3-Hywind spar-buoy	Pitch	1.580	−0.084	0.066	1.930	−0.116	0.077	3.113
		Yaw	−0.021	0.091	0.108	1.983	−0.036	0.120	3.429
	MIT/NREL TLP	Surge	1.206	0.436	0.016	−0.831	−0.222	0.077	3.018
2	ITI Energy barge	Pitch	1.722	−0.637	0.065	−0.381	1.677	0.077	1.835
3	ITI Energy barge	Pitch	0.939	1.518	0.066	2.132	2.979	0.078	6.863
	OC3-Hywind spar-buoy	Pitch	3.324	11.961	0.029	0.420	0.000	0.000	0.000
		Yaw	−0.222	2.000	0.029	−0.359	3.185	0.058	3.385
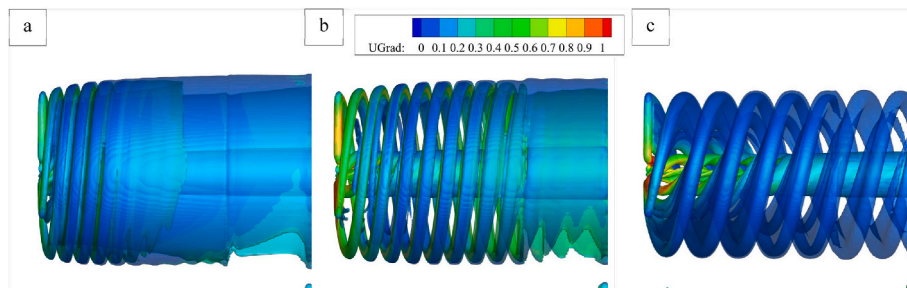
Fig. 6. Iso-surface of Q = 0.001and 0.0001 colored by velocity gradient magnitude for Monopile in a) Below-rated, b) Rated; c) Above-rated.

behavior is as expected. Increasing the wind speed leads to expanding the distance among the helical rings. The helical geometry disappears sooner for cases with a higher tip speed ratio as the gap between vortex rings is smaller, a fact that promotes turbulent wake mixing. Moreover, the wake expansion in the radial direction for the highest wind speed is less due to the higher axial flow momentum in this operating condition.

The available literature for comparison [59,68] focused on the below-rated regime. Therefore, the current paper first investigates this suitable condition for comparison particularly and then expands the study into the rated and above-rated ones. In Fig. 7, the variation of rotor thrust affected by the multiple-DoF motion of ITI Energy barge and OC3-Hywind spar-buoy platforms are compared with the monopile case. The current ALM code is compared with the NVLM code by Lee et al. [59] and the FWVR code by Dong et al. [68]. Since in Lee's simulation the platform motions start after about one rotor rotation, their data are shifted −360° along the azimuth angle axis. The results of the monopile case revealed that there is a 2.9% difference between the current code and the NVLM code and a 1.4% difference with the FWVR code. For the other platforms, the results follow a similar trend, and the thrust amplitudes and frequencies of the three methods are quite close. The

interesting point to notice is the sharpness of the extrema. The local maximum often occurs when the rotor has its relatively maximum speed in the opposite direction of wind flow, while the local minimum usually happens when the platform speed in the wind direction is maximum. Sebastian et al. [69] investigated the time lag effects on rotor performance in more detail. As discussed in a previous paper by the current authors [29], the dynamic stall addresses the presence of flattening in forwarding motion, while in the backward motion it can be produced by the turbulent wake state or even the vortex ring state. The current ALM code shows its ability to capture the phenomena like vortex ring state that are not considered by the lower fidelity methods [29].

Table 5 summarizes the mean (μ) value and standard division (σ) of power and thrust normalized by correspondent data of the monopile case. Numbers for the ITI case reveals standard deviations of 0.57 for the normalized power and 0.25 for the normalized thrust, which are significant. Furthermore, there are differences even in mean values, as while the mean power increased by 6.3%, the thrust decreased by about 1.5%. Simulation shows no considerable change in mean values for the other two platforms. However, there are notable variances, with a standard deviation ranging from 1.4 to 3.7%. Data demonstrates power has a standard deviation double that of thrust.

Different rotor data were reported for each of the four platforms, as shown in Fig. 7 and Table 5. As expected, the output of ITI platform is influenced significantly more than the other platforms. The ITI platform is a relatively cheap and simple construction composed of a barge platform and eight catenary mooring lines. The large waterplane area provides a recovery moment that maintains the platform stability and
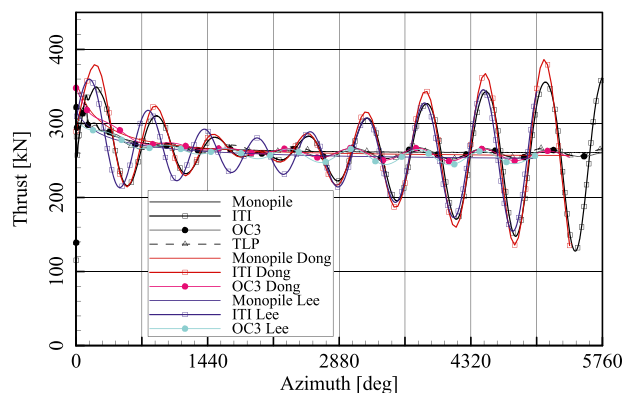

Fig. 7. Variation in the rotor thrust for different platform configurations in the below-rated condition.

Table 5

Summary of mean and standard deviation values for relative power and thrust for different platforms.

Operating conditions.	Floating platform	Normalized Power		Normalized Thrust	
		μ	σ	μ	σ
1	ITI Energy barge	1.0630	0.5752	0.9842	0.2512
	OC3-Hywind spar-buoy	0.9997	0.0331	0.9994	0.0142
	MIT/NREL TLP	1.0005	0.0372	1.0001	0.0160

avoids capsizing the entire floating foundation under harsh sea conditions. Catenary mooring lines prevent the drift of the floating foundation. However, the platform suffers from considerable platform motion due to its relatively shallow draft. On the other hand, the OC3-Hywind spar-buoy is influenced by the see wave to a lesser degree. In fact, this platform consists of a slender spar buoy moored by three catenary lines. The restoring moment is provided by ballast weights that shift the mass center below the buoyancy center. The deep draft helps achieve static stability in the presence of waves and wind loads. Finally, the MIT/NREL TLP platform shows the highest stability among the platforms. This model features high-tension lines connecting the buoyant substructure and anchoring structures. The tension provided by buoyancy produces an effective restoring moment that lessens the undesirable responses to the waves and wind loads.

Fig. 8 visualizes the side view (x-z plane) of the wake structure behind the monopile and the three floating platforms in the below-rated condition. This figure illustrates how the motion of each platform influences the flow field. The wake behind the monopile case was initially formed in a shape of a well-defined helical geometry, and after maintaining the vortex rings over a downstream distance of 2-3D, it decays into the turbulent wake. In contrast, the emitted wakes behind the turbines with floating platforms have entirely different structures with periodic variations in the vortex strength.

In general, the contours show that the helical propagation of the wake in floating platforms lasted less than in the monopile case and the wakes propagate in circles rather than in spiral shapes. Such a wake evolution phenomenon was also observed in Refs. [70,71]. This is due to the interaction between the helical blade tip vortices, which pairs and merges the tip vortices and produces rings with stronger vorticities. As it can be observed, the stronger circles in Fig. 8-b:d takes a longer time than Fig. 8-a to decay. It should be mentioned this evolution is probable even for the fixed cases, in spite of this, the oscillation of vortices distances due to the streamwise motion of the platform [40] and oscillation in tip vortices strength due to changes in the angle of attack both can increase the probability.

The most perturbed wake is associated with the ITI Energy barge case and then the OC3-Hywind spar-buoy platform. It was indicated that even though the turbine performance did not influence much for the OC3-Hywind spar-buoy and the MIT/NREL TLP platforms, they yielded highly unsteady wake structures. This reveals that even small amplitudes of motion can result in considerable wake deformation. The emitted vortices interact with other vortices and influence each other during the wake convection. Interactions and merging vortex rings are observed even for the MIT/NREL TLP platform.

The effect of remarked platform motions on the thrust force of the NREL 5 MW rotor are presented in Fig. 9. In these plots, the rotor's thrust force variations undergoing individual translational and rotational motions are reported in a time domain. Data of monopile case is compared with six modes of movement mentioned in Table 2 for below-rated operating conditions. The data indicates that the rotor thrusts fluctuate around their mean values after an initial transition. The initial transition is addressed by the wake development around the rotor that causes a blockage effect in front of the rotor by decreasing the inflow speed. It is apparent that the pitch motion of the ITI Energy barge and then other pitch and surge motions led to the most significant variations, while the other motions had relatively little effect on the output. According to previous study [29], the pitch and surge platform motions are streamwise, hence the relative velocity between the blades and the incoming wind is periodical. This results in more periodic aerodynamic load and, subsequently, periodic vorticity strength [29].

Fig. 10 compares the effect of each remarked platform motions on the wake for the ITI Energy barge. Figure a) represents the heave, b) the surge, and c) the pitch motion as stated in Table 4. The combination of these three motions is demonstrated in Fig. 10-d. As seen in Fig. 10-a, the wake shape is similar to a crankshaft due to the vertical movement of the platform. Fig. 10-b shows that the horizontal movement of the platform
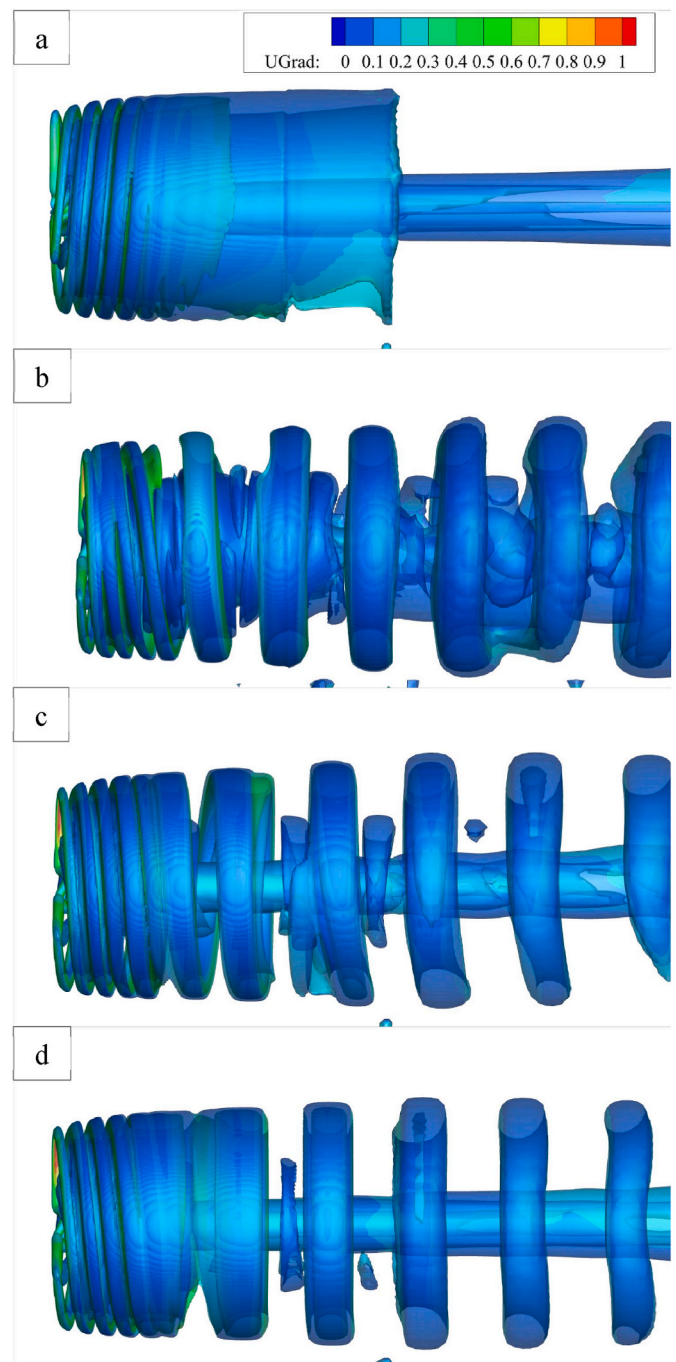

Fig. 8. Iso-surface of Q = 0.001and 0.0001 colored by velocity gradient magnitude for a) Monopile, b) ITI Energy barge; c) OC3-Hywind spar-buoy; d) MIT/NREL TLP.

leads to pairing rings into one and shaping new rings with different strengths. The pitching case revealed a more perturbed and complex helical shape among the three separate motions. The ITI Energy barge case with multi-degrees of motion, shown in Fig. 10-d, is more similar to the case with just the pitch that indicates it is influenced most by the pitch motion.

In order to demonstrate the effect of wake structure on the downstream velocity field, the flow velocity contours behind the platforms at the below-rated condition are visualized in Fig. 11. The contours are reported for four sections at distances of x/D equal to 0, 2, 4, and 6 where x is the downstream distance. The contours were colored by streamwise velocity (u_x) and the areas with $|u_y|$ and $|u_z|$ bigger than 0.25
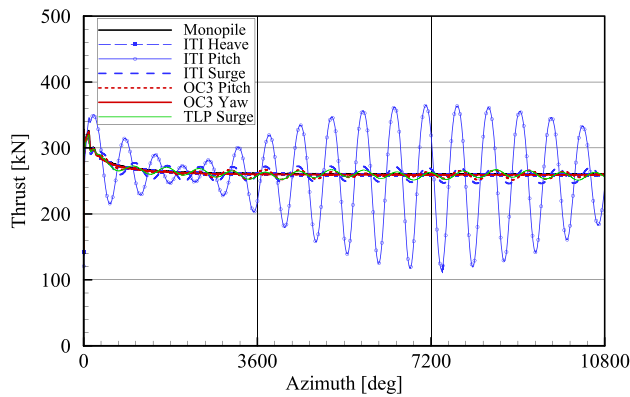
Fig. 9. Variation in the rotor thrust for different platform motions.

are highlighted with blue and red lines respectively.

In general, while for the monopile case the velocity distribution is axisymmetric concerning the wake age, this becomes disordered, particularly for the ITI Energy barge platform. The portion of contour in dark blue is important, which is comparatively larger for the monopile case. It is noticeable that, as strong wake vortices pass the downstream region, a non-axisymmetric induced velocity region appeared for the floating cases. A similar non-axisymmetric core was reported for the yawed wind turbine [35,72]. The highlighted areas in the counters indicated that while the $|u_y|$ and $|u_z|$ are fairly non-axisymmetric at all sections for the ITI platform, the non-asymmetricity appeared just in the farthest section for the OC3-Hywind spar-buoy and MIT/NREL TLP platforms. A non-asymmetric distribution is crucial from a downstream wind turbine perspective since it can impose an unbalanced load on the downstream inline rotor. Accordingly, besides the wake helical shape, the vortex strength variation in the azimuthal direction is important.

The vortex strength depends on the Reynolds number and local α of the upstream blade sections. In Fig. 12, the variation of α along the blade-1 during the initial 10 min is reported. Data for the monopile case are compared with the mentioned three floating platforms. The x and y directions are, respectively, time and the spanwise blade position, and the contours are colored by the calculated angle of attack based on the sampled velocity from the flow field. It should be mentioned that the tilt

angle and tower are omitted to focus on the platform motion effects.

As expected, the calculated angle of attack for the monopile cases are nearly constant at all of the three operation conditions. Due to a higher wind speed at the rated condition, α is comparatively higher than the below-rated condition. Therefore, while a higher lift coefficient is provided, the angle of attack is closer to the stall criteria. For the above rated condition applying a pitch angle of 15° reduced the angle of attack to under 5° for roughly half of the blade.

The most striking observation to emerge from the contours is that while the blade angle of attack for the monopile platform was almost constant, it varied considerably for the floating platforms over time. The affected angle of attack and relative velocity by the platform motion contribute to the flow field deformation and temporal effects on induced velocity [69]. The displacements of the floating platforms are also plotted using white lines to indicate the relation between the motion and α variations. The displacements are normalized by the maximum value ($|A_1|+|A_2|$) and offset to zero by modifying the value of X_0 into zero.

Among the floating platforms, significant variations are observed for the ITI cases. As it can be seen in Fig. 12-OI ITI, the blade experiences negative α values in some spanwise sections. Fundamentally, when a rotor imparts energy into the flow, it is operating in a propeller or quasi-propeller state, and when it extracts energy from the flow, it is operating in the windmill state. The thrust for the ITI case was positive because just a portion of blades experienced a negative angle of attack. Undergoing the rotor into the turbulent wake state is an occurrence in which momentum theory, and therefore BEM, is no longer valid. Conventionally these states are defined based on the rotor induced velocity ratio and the rotor thrust [29,73]. Considering Fig. 12-OI ITI, as the pitch motion moves the platform in the forward direction, the angles of attack decrease.

It is evident that the forward and backward motion of the turbine affects the velocity triangle and hence the forces. Less obvious is the temporal effect that local thrust has on the local flow and inflow velocity. Furthermore, at higher displacement amplitude or frequency, the blade may touch the vortex omitted by the preceding blade and by influencing the inflow turbine goes into turbulence state or even vortex ring state. Meanwhile, the local thrust force variation results in a more perturbed wake. These points emphasize the significance of wake simulation in floating turbines utilizing ALM.

The platform movement in the rated condition is more problematic due to a closer α to the stall criteria. Even a small change of α can lead to
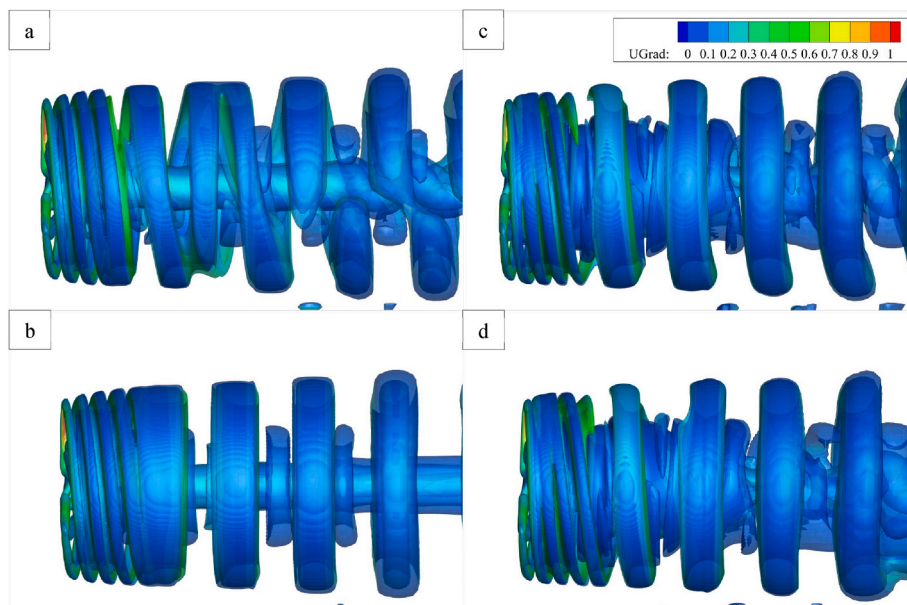

Fig. 10. Iso-surface of Q = 0.001and 0.0001 colored by velocity gradient magnitude for ITI Energy barge a)Heave, b) Surge; c) Pitch; d) The three degrees of motion.
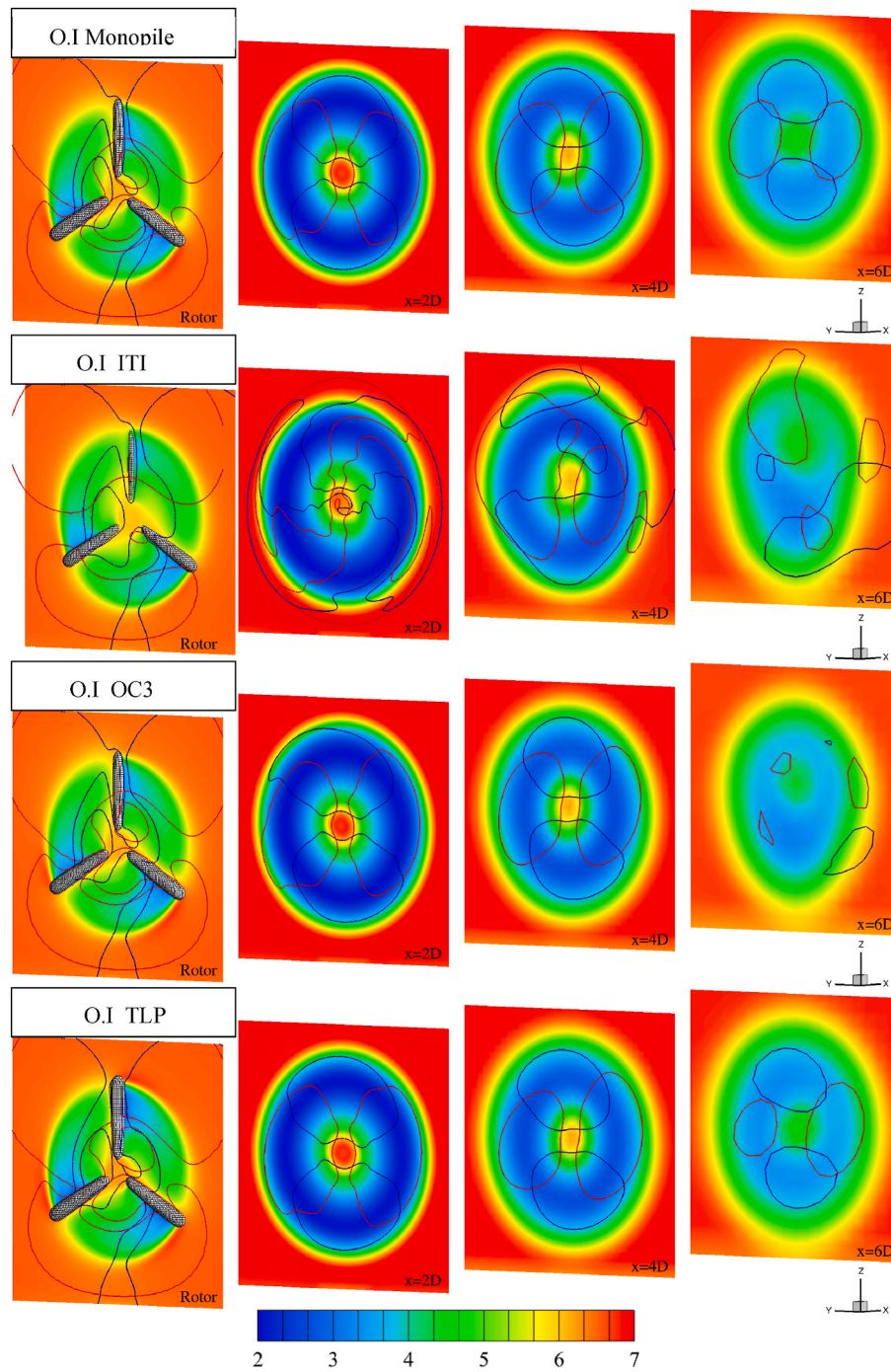
Fig. 11. Contours of x velocity at $x/D = 0$, 2,4 and 6, for the below-rated cases.

considerable lift and drag variation and consequently producing a distinct form of wake. The blade design for offshore turbines needs to consider the potential variation of the angle of attack due to the platform motion. Since the calculation of the angle of attack is straightforward by ALM, it provides a promising tool for blade design optimization in offshore wind farms. Based on Fig. 12-OII ITI, undergoing the blades of ITI case into stall condition is probable because of close angle of attack to the corresponding stall criteria at rated condition. However, considering the blade twist, the blade of the rated ITI case is not undergoing a deep static stall.

Fig. 12-OIII ITI shows that utilizing the pitch-controlled system decreased the α, nonetheless similar to the below-rated and rated ITI cases, frequency and amplitude of variation are in consistence with the

platform pitch motion. Fig. 12-OI OC3 and TLP indicate the α variation for OC3 and TLP platforms in the below-rated condition is insignificant, although it was showed even those small displacements are enough to reform the wake shape (see Fig. 8). The above-rated OC3 case revealed a remarkable superposition of motions. Fig. 12-OIII OC3 indicates the superposition of one pitch frequency and the two yaw frequencies generates seven fluctuations in the angle of attack.

Comparing the ALM result with LES for the NREL Phase VI case reveals the promising capabilities of the ALM code in the simulation of near to far wake development (see Fig. 5). To further prove this statement, the wake evolution of the floating NREL 5 MW cases is studied in Fig. 13. In this figure, the wake recovery in terms of velocity deficit is depicted along the streamwise direction at five lateral distances of $y/r =$
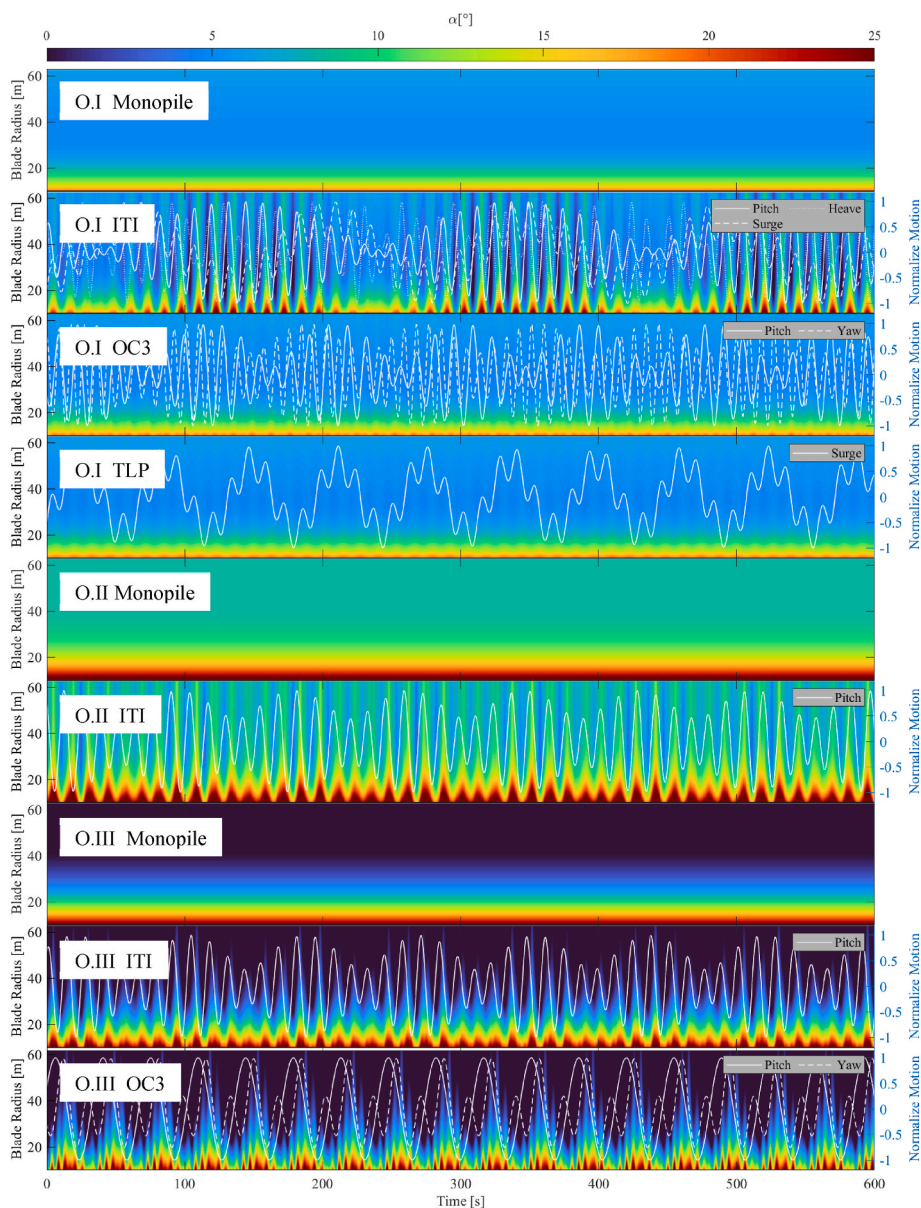
Fig. 12. Contour for the time evolution of angle of attack along the blade and the plot for normalized motions.

0, 0.5, 1, 1.5 and 2 to facilitate a more quantitative comparison. Data are reported for the six floating cases introduced in Table 4, along with the monopile cases at the three operating conditions. In this figure, colors indicate the type of platforms, and operation and environment conditions of 1, 2, and 3 are indicated by no symbol, circle symbols, and delta symbol, respectively.

Fig. 13 confirms the influence of floating motions on wake recovery. In a general sense, wake recovery is affected by platform, operation, and environmental conditions. For all cases, the velocity magnitude tends to recover its upwind values by getting far from the rotor, albeit at different rates. The results show that the maximum velocity fluctuation amplitude does not always occur immediately behind the rotor, and the fluctuation amplitude may amplify at further downstream (Fig. 13-b).

A velocity decrease is seen up to the blade's radius, and beyond that, the velocity magnitude increases. Nonetheless, there is an exception at the center line as the velocity increases for all below-rated and rated cases. This is due to the passing flow through the rotor center. Since the hub and nacelle avoid passing flow in an actual wind turbine, this is an error of simulation that is present in the simulation methods that consider no hub and nacelle. Even though this effect might be

technically negligible to study, and many researchers reported just beyond the root area [28], one aim of the current paper is the declaration of both cons and pros of the ALM method, helping other researchers to choose appropriate tools based on their requirements. Hub and nacelle can be considered as body forces, but calibration of the actuator elements requires more reference data [74].

Considering the below-rated cases, all of the monopile, ITI, OC3, and TLP cases show a similar trend, although there is a dramatic fluctuation in the velocity magnitude deficit for the ITI case. By approaching the tip, the deviation of the OC3 platform from the monopile becomes larger due to the angular movement of the platform and the higher sensibility of the angle of attack at the tip [29]. The result of TLP is quite close to monopile due to the limited surge movement of this platform. From Fig. 13-b and -c for the ITI platform in below-rated condition, the wavelength of fluctuation increases by getting far from the rotor due to vortex pairing. Hence, there is no considerable contribution from fluctuation to recover flow faster by making the flow field more perturbed.

While the most influenced lateral distance for the below-rated cases is at the blade tip distance, no considerable velocity deficit is determined for the above-rated cases there, and in the rated conditions, the most
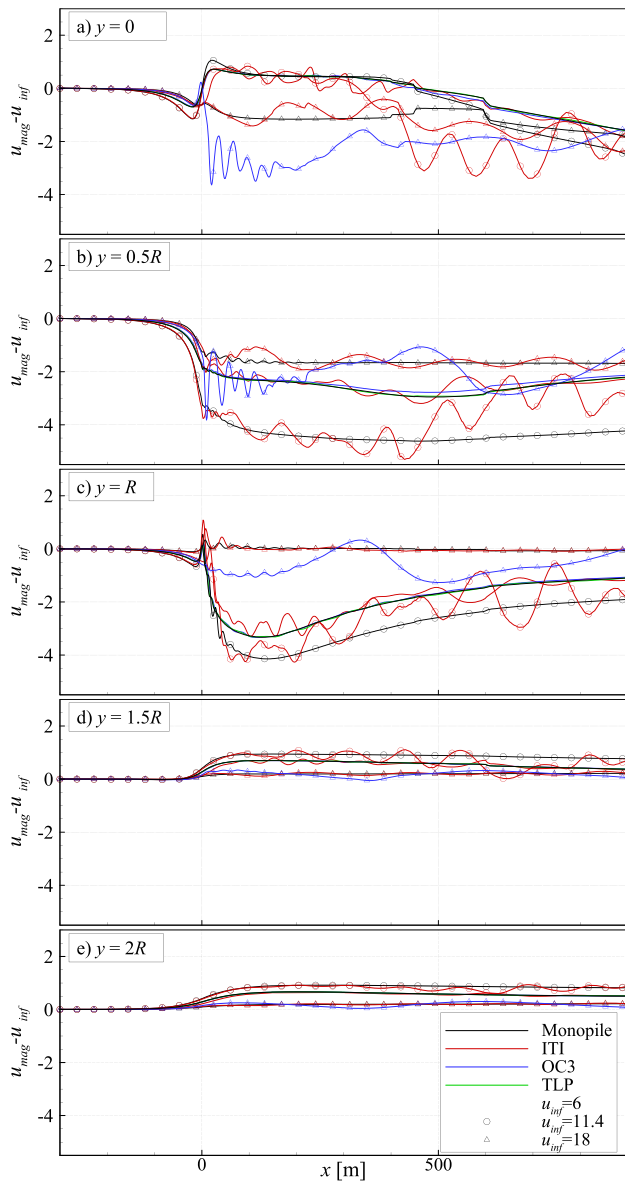
Fig. 13. Wake recovery in terms of velocity deficit along the streamwise direction at five different lateral distances of $y/r = 0, 0.5, 1$, 1.5 and 2 (a–e).

influenced flow field was observed at the middle blade distance. Presence of fundamental difference between the operation conditions requires to be analyzed. Thus, the influence of the operating conditions is first determined to distinguish the effects of operating conditions from the impact of platform type. After clarification of the operation condition effects, the data of each floating platform are compared with theirs corresponding monopile case.

Based on Fig. 13, the velocity deficit is larger at the rated condition, and there is significantly higher unsteadiness in the wake of the ITI platform compared to the other examined cases. Fig. 14 shows how the development of the velocity deficit profile differs between the three operation and environment conditions. The lateral velocity deficit profiles through the hub level for the monopile case are plotted at streamwise distances of $x/d = 1, 2, 4$ and 8 downstream. The profiles are extremely distinct among the different operation conditions. The highest velocity deficit region behind the rotor is due to tip vortex shedding, however, by increasing the wind velocity from 6 to 18 m/s, the W-shaped velocity deficit profile concentrates toward the blade root. This results from a higher flow Reynolds number and the turbine pitch
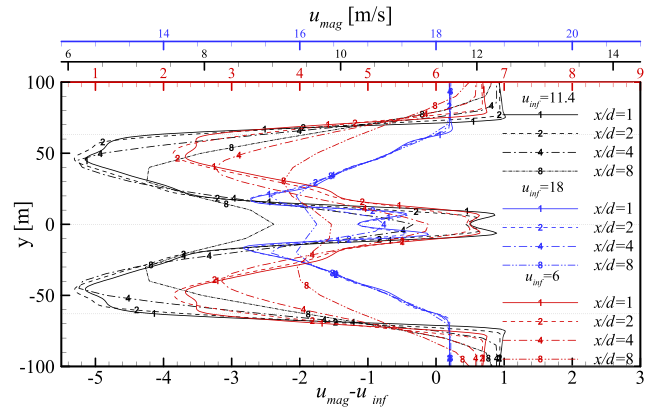

Fig. 14. The velocity deficit profile of monopile case at the below-rated condition (red), rated condition (black), and above-rated condition (blue).

control.

In the above-rated condition, momentum loss is not the highest potential due to less energy extraction. The high Reynolds number flow leads to a high shear between the ambient and wake regions, breaking down the vortical structures into instabilities. For the below-rated and rated conditions, the highest velocity deficit was at blade tip distance, and by moving toward downstream, these extremum gets closer to the centerline. For both cases, the highest velocity deficit increased from the distance of $x/d = 1$ to 2 and then it followed by continues decrease toward downstream. Comparing the profiles at $x/d = 4$, indicates the rate of wake recovery is less for the rated case that is associated with the relatively higher momentum loss in the rated condition.

As reported in Fig. 13, the floating ITI platform deviates significantly from the monopile case in the rated condition. To study the rated cases in more detail, velocity magnitude along the streamwise direction and the lateral velocity deficit profiles through the hub level are plotted in Fig. 15. The velocity magnitude is plotted in Fig. 15-A for three heights of rotor center ($z = 0$), R/2, and R above that. As it can be seen, the velocity magnitude at the center is quite similar up to 2.5D downstream; however, it is followed by a drop ($x = 3D$ to 4D) and then a dramatic fluctuation. Unlike the below-rated condition, where for the ITI case paring root vortexes results in mixing flow and vortex decay, in the rated
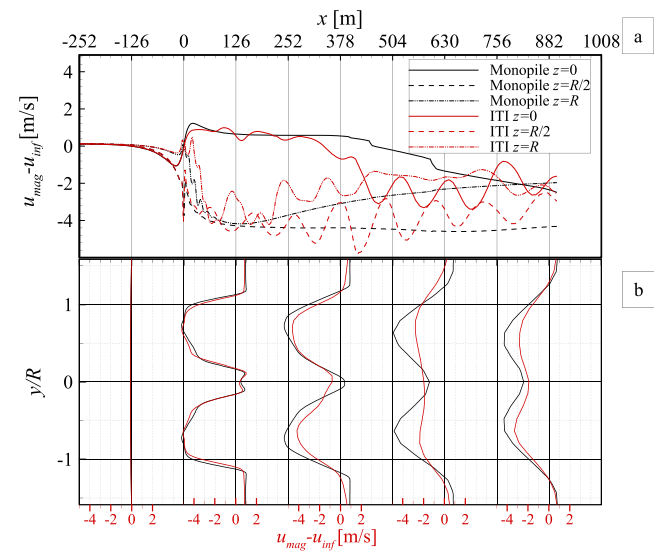

Fig. 15. Wake recovery in terms of velocity magnitude along streamwise direction and velocity deficit profile as a function of lateral distance for the rated cases.

condition, vortex paring leads to considerable instability in the center line.

For the middle blade radial distance ($z=R/2$), the reported data for the floating ITI platform fluctuates significantly compared to the monopile case. The fluctuation amplitude is up to 3 [m/s], and its wavelength is almost 114 [m], which shows that each fluctuation period consists of 6 blade vortices. From 5D downstream, the velocity magnitude is higher than the monopile, which shows the movement helped wake recovery in terms of velocity deficit, although with considerable oscillation. The velocity deficit profiles at different distances from downstream are plotted in Fig. 15-B. Comparing the velocity deficit profiles might indicate an emphasized wake recovery due to the more perturbed flow; however, Fig. 15-A shows that there is a massive fluctuation that is potentially even a bigger issue. The dramatic effect of floating motion on the downstream flow field proves the importance of unsteady simulation.

Data for the above-rated condition are reported for the monopile, ITI, and OC3 cases in Fig. 16. The point that distinguishes the above-rated condition is that due to the higher distance of about 30 [m] between vortex rings, vortex pairing phenomena is less probable in this condition. Despite this fact, as shown in Fig. 16, the velocity magnitude at the centerline oscillates with a wavelength of about 205 [m] for the ITI case and 600 [m] for the OC3 case. The velocity deficit profiles show that the center of the W-shape profiles are not at the center line for the floating platforms. This is a vortex meandering phenomenon that is enhanced by the platform floating moment.

The motion of the OC3 in the above-rated condition is comparatively more complex as it follows two angular motions of pitch and yaw. Because of the angular platform motion, the velocity of the blade element and the angle of attack depend on the distance of the element from the motion center and the current azimuth angle. In other words, the inflow velocity normal to the rotor plane for each blade element is different even at a certain time and depends on the element height or lateral distance (see Fig. 17). As a consequence, the emitted wake from the rotor bottom, top, right, and left sides of the rotor are different, and the downstream velocity follows distinct trends for each part of the same annular ring.

Unlike the OC3 case in the below-rated condition, where the wake was dominated by pitch, here, due to a higher yaw motion, the flow field is influenced by both, creating a complex wake that emphasizes the significance of unsteady simulation with multi DoF motions. Because
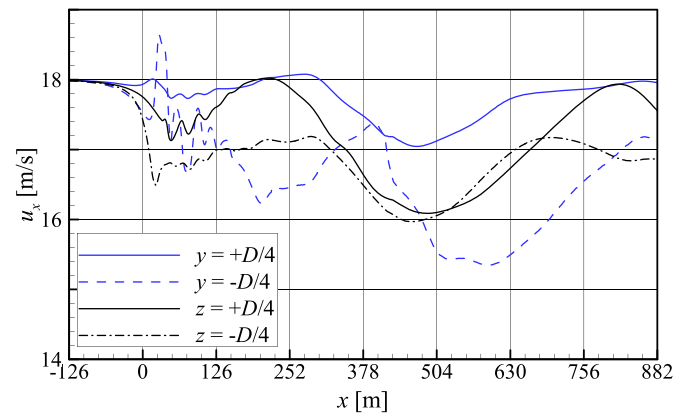

Fig. 17. Velocity along the streamwise direction at the distance of D/4 from the centerline for four different locations.

BEM and ADM discretize the turbine into circumferentially averaged rings, they cannot simulate angular platform motion in their original form [25,75].

5. Conclusions

This paper made an effort to determine the unsteady effects due to platform multi-motion on a turbine's aerodynamic and near-to-far wake deformation. An ALM code was developed to investigate the NREL 5 MW wind turbine with different platforms, operations, and environmental conditions listed in the test matrix. Initially, the reliability of the ALM code was examined through three sets of validation studies for turbine output in fixed and floating conditions and the wake expansion in terms of size and rate. Despite the reduced computational effort compared to the blade-resolved CFD solutions the results showed that the flow field, vorticity trajectories, and wake are well captured. In contrast to steady approaches, ALM captures the unsteadiness due to blade rotation, particularly a non-axisymmetric velocity deficit profile, even for the monopile cases.

Analyzing the monopile platform at the three operating conditions revealed that by increasing the TSR the helical geometry decays sooner as the pitch gap between vortex rings gets closer, which promotes turbulent wake mixing. While the most influenced lateral distance for the below-rated cases was at the blade tip distance, no considerable velocity deficit was determined there for the above-rated cases, and the most influenced flow field in the rated conditions was observed at the middle blade distance. The rate of wake recovery is less for the rated case, which is associated with the relatively higher momentum loss in the rated condition. The result of TLP was quite close to monopile due to the limited surge movement of this platform. The most influenced turbine output was reported for the ITI platform, which has a cheaper structure and lower stability.

Since the motion of each floating platform varies by operation conditions, different turbine outputs and wakes were calculated. It is noticeable that, as strong wake vortices pass the downstream region, a non-axisymmetric induced velocity region appears for the floating cases. A non-asymmetric distribution is crucial from a downstream wind turbine perspective since it can impose an unbalanced load on the downstream inline rotor. Accordingly, besides the wake helical shape, the vortex strength variation in the azimuthal direction is important. The vortex strength depends on the Reynolds number and local α of the upstream blade sections. The affected angle of attack and relative velocity by the platform motion contribute to the flow field deformation and temporal effects on induced velocity.

The results showed that the maximum amplitude of fluctuating velocity deficit does not always occur immediately behind the rotor, and it might be amplified further downstream. The motion of platforms can
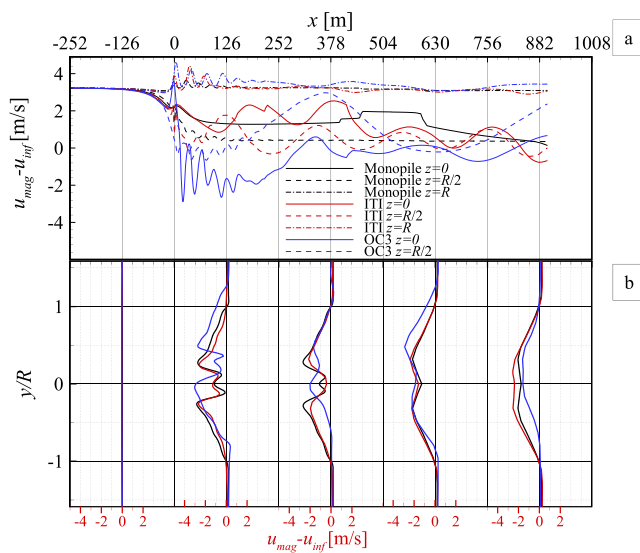

Fig. 16. Wake recovery in term of velocity magnitude along streamwise direction and velocity deficit profile as a function of lateral distance for the above-rated cases.

transform wake propagation into the form of stronger circles rather than spiral shapes by pairing vortices. Vortex pairing is enhanced by the oscillation of the pitch distances for the streamwise platform motions, particularly in pitch and surge motion, also with oscillation of vortices strength due to variation in relative velocity as it happens in yaw motion. Investigating the TLP platform in below-rated conditions revealed that even small amplitudes of motion can result in considerable wake deformation. The results of the ITI platform at the rated condition showed that although from 5D downstream, the average velocity magnitude is higher than the monopile, there is a massive fluctuation that is potentially even a more significant issue. Hence, fluctuation does not contribute considerably to recovering flow faster by making the flow field more perturbed.

The complexity of angular platform motions is an important issue of floating platforms that is missed in circumferentially averaged approaches, including the original form of BEM and ADM. Comparing each remarked platform motion of the ITI case showed the pitching motion reveals a more perturbed and complex helical shape among the three separate motions. Besides the fact that the amplitude of this motion is typically higher, the angular movements result in a different relative velocity based on the azimuthal position of the blade section. As shown for the OC3 platform, even at the below-rated condition by approaching the tip, the deviation of the OC3 platform from the monopile becomes larger due to the angular movement of the platform and the higher sensibility of the angle of attack at the tip. The OC3 platform motion at the above-rated condition is comparatively more complex as there is a remarkable superposition of two angular motions of pitch and yaw. The emitted wake from the rotor bottom, top, right, and left sides are different, and the downstream velocity follows distinct trends for each part of the same annular ring.

It is also worth mentioning that the platform movement in the rated condition is more problematic due to a closer α to the stall criteria. Even a small change of α can lead to considerable lift and drag variation and consequently produce a distinct form of the wake. The blade design for offshore turbines needs to consider the potential variation of the angle of attack due to the platform motion. Also, being subject to negative α values in some spanwise sections of the ITI case emphasizes utilizing a method that can simulate the blade interaction with the vortex omitted by the preceding blade as the turbine might undergo a turbulence state or even vortex ring state. In sum, the dramatic effect of the multi-DoF motion of a floating platform on the downstream flow field emphasizes the significance of unsteady simulation with multi-DoF motions and avoiding circumferentially averaged rings. Future research will focus on the effects of unsteady wake on the downstream wind turbine. In this regard, it is vital to place a floating wind turbine at different positions.

Data availability

Data is available on request. Requests can be sent to the corresponding author's Email.

CRediT authorship contribution statement

Alireza Arabgolarcheh: Conceptualization, Methodology, Simulation, Formal analysis, Writing – original draft. **Amirhossein Rouhollahi:** literature, Writing – review & editing, introduction. **Ernesto Benini:** Conceptualization, Supervision, Writing – review & editing.

Declaration of competing interest

The authors declare that they have no known competing financial interests or personal relationships that could have appeared to influence the work reported in this paper.

References

[1] P. Sadorsky, Wind energy for sustainable development: driving factors and future outlook, J. Clean. Prod. 289 (2021), 125779, https://doi.org/10.1016/j.jclepro.2020.125779.

[2] M. Bilgili, H. Alphan, Global growth in offshore wind turbine technology, Clean Technol. Environ. Pol. (2022), https://doi.org/10.1007/s10098-022-02314-0.

[3] S. Watson, A. Moro, V. Reis, C. Baniotopoulos, S. Barth, G. Bartoli, F. Bauer, E. Boelman, D. Bosse, A. Cherubini, A. Croce, L. Fagiano, M. Fontana, A. Gambier, K. Gkoumas, C. Golightly, M.I. Latour, P. Jamieson, J. Kaldellis, A. Macdonald, J. Murphy, M. Muskulus, F. Petrini, L. Pigolotti, F. Rasmussen, P. Schild, R. Schmehl, N. Stavridou, J. Tande, N. Taylor, T. Telsnig, R. Wiser, Future emerging technologies in the wind power sector: a European perspective, Renew. Sustain. Energy Rev. 113 (2019), 109270, https://doi.org/10.1016/j.rser.2019.109270.

[4] D. Micallef, A. Rezaeiha, Floating offshore wind turbine aerodynamics: trends and future challenges, Renew. Sustain. Energy Rev. 152 (2021), 111696, https://doi.org/10.1016/J.RSER.2021.111696.

[5] T. Asim, S.Z. Islam, A. Hemmati, M.S.U. Khalid, A review of recent advancements in offshore wind turbine technology, Energies 15 (2022), https://doi.org/10.3390/en15020579.

[6] K.A. Shah, F. Meng, Y. Li, R. Nagamune, Y. Zhou, Z. Ren, Z. Jiang, A synthesis of feasible control methods for floating offshore wind turbine system dynamics, Renew. Sustain. Energy Rev. 151 (2021), 111525, https://doi.org/10.1016/j.rser.2021.111525.

[7] J. Chen, M.-H. Kim, Review of recent offshore wind turbine research and optimization methodologies in their design, J. Mar. Sci. Eng. 10 (2021) 28, https://doi.org/10.3390/jmse10010028.

[8] K. Jahani, R.G. Langlois, F.F. Afagh, Structural dynamics of offshore Wind Turbines: a review, Ocean Eng. 251 (2022), 111136, https://doi.org/10.1016/j.oceaneng.2022.111136.

[9] Y. Liu, Q. Xiao, A. Incecik, C. Peyrard, D. Wan, Establishing a fully coupled CFD analysis tool for floating offshore wind turbines, Renew. Energy (2017), https://doi.org/10.1016/j.renene.2017.04.052.

[10] M. Hansen, Aerodynamics of Wind Turbines, third ed., Routledge, 2015 https://doi.org/10.4324/9781315769981.

[11] National Renewable Energy Laboratory, OpenFAST v3.2.0 Documentation, 2022.

[12] A. Manjock, Design Codes FAST and ADAMS® for Load Calculations of Onshore Wind Turbines, Ger. Lloyd Wind. GmbH, 2005. Rep. No. 72042.

[13] J.M. Jonkman, D. Matha, Dynamics of offshore floating wind turbines-analysis of three concepts, Wind Energy 14 (2011) 557–569, https://doi.org/10.1002/we.442.

[14] T. Sebastian, M.A. Lackner, Characterization of the unsteady aerodynamics of offshore floating wind turbines, Wind Energy 16 (2013) 339–352, https://doi.org/10.1002/WE.545.

[15] X. Li, C. Zhu, Z. Fan, X. Chen, J. Tan, Effects of the yaw error and the wind-wave misalignment on the dynamic characteristics of the floating offshore wind turbine, Ocean Eng. 199 (2020), 106960, https://doi.org/10.1016/j.oceaneng.2020.106960.

[16] D. Matha, S.-A. Fischer, S. Hauptmann, P.W. Cheng, D. Bekiropoulos, T. Lutz, T. Duarte, K. Boorsma, Variations in ultimate load predictions for floating offshore wind turbine extreme pitching motions applying different aerodynamic methodologies, in: Twenty-Third Int. Offshore Polar Eng., . Conf., OnePetro, 2013.

[17] A. Arabgolarcheh, E. Benini, M. Anbarsooz, Development of an actuator line model for simulation of floating offshore wind turbines, Am. Soc. Mech. Eng. Power Div. POWER. (2021), https://doi.org/10.1115/POWER2021-60098, 2021-July.

[18] J. Katz, A. Plotkin, Low-speed Aerodynamics, Cambridge university press, 2001.

[19] X. Shen, J. Chen, P. Hu, X. Zhu, Z. Du, Study of the unsteady aerodynamics of floating wind turbines, Energy 145 (2018) 793–809, https://doi.org/10.1016/j.energy.2017.12.100.

[20] X. Shen, P. Hu, J. Chen, X. Zhu, Z. Du, The unsteady aerodynamics of floating wind turbine under platform pitch motion, Proc. Inst. Mech. Eng. Part A J. Power Energy. 232 (2018) 1019–1036, https://doi.org/10.1177/0957650918766606.

[21] S.N. Rodriguez, J.W. Jaworski, Strongly-coupled aeroelastic free-vortex wake framework for floating offshore wind turbine rotors. Part 1: numerical framework, Renew. Energy 141 (2019) 1127–1145, https://doi.org/10.1016/j.renene.2019.04.019.

[22] S.N. Rodriguez, J.W. Jaworski, Strongly-coupled aeroelastic free-vortex wake framework for floating offshore wind turbine rotors. Part 2: application, Renew. Energy 149 (2020) 1018–1031, https://doi.org/10.1016/J.RENENE.2019.10.094.

[23] A. Otter, J. Murphy, V. Pakrashi, A. Robertson, C. Desmond, A review of modelling techniques for floating offshore wind turbines, Wind Energy (2021), https://doi.org/10.1002/we.2701.

[24] R. Mikkelsen, Actuator disc methods applied to wind turbines, Technical University of Denmark, 2004, 109 p. (MEK-FM-PHD; No. 2003-02), https://orbit.dtu.dk/en/publications/actuator-disc-methods-applied-to-wind-turbines. (Accessed 27 October 2020).

[25] J.B. De Vaal, M.O.L. Hansen, T. Moan, Effect of wind turbine surge motion on rotor thrust and induced velocity, Wind Energy 17 (2014) 105–121, https://doi.org/10.1002/we.1562.

[26] D. Micallef, T. Sant, Loading effects on floating offshore horizontal axis wind turbines in surge motion, Renew. Energy 83 (2015) 737–748, https://doi.org/10.1016/j.renene.2015.05.016.

[27] K.M. Kopperstad, R. Kumar, K. Shoele, Aerodynamic characterization of barge and spar type floating offshore wind turbines at different sea states, Wind Energy 23 (2020) 2087–2112, https://doi.org/10.1002/WE.2547.

[28] A. Rezaeiha, D. Micallef, Wake interactions of two tandem floating offshore wind turbines: CFD analysis using actuator disc model, Renew. Energy 179 (2021) 859–876, https://doi.org/10.1016/J.RENENE.2021.07.087.

[29] A. Arabgolarcheh, S. Jannesarahmadi, E. Benini, Modeling of near wake characteristics in floating offshore wind turbines using an actuator line method, Renew. Energy 185 (2022) 871–887, https://doi.org/10.1016/j.renene.2021.12.099.

[30] N. Troldborg, Actuator line modeling of wind turbine wakes (accessed June 17, 2019), http://orbit.dtu.dk/en/publications/actuator-line-modeling-of-wind-turbine-wakes (5ba63e95-7f74-4e6c-82b8-9f497315a664).html), 2009.

[31] J.N. Sørensen, R.F. Mikkelsen, D.S. Henningson, S. Ivanell, S. Sarmast, S. J. Andersen, Simulation of wind turbine wakes using the actuator line technique, Philos. Trans. R. Soc. A Math. Phys. Eng. Sci. 373 (2015), 20140071, https://doi.org/10.1098/rsta.2014.0071.

[32] D.D. Apsley, P.K. Stansby, Unsteady thrust on an oscillating wind turbine: comparison of blade-element momentum theory with actuator-line CFD, J. Fluid Struct. 98 (2020), 103141, https://doi.org/10.1016/j.jfluidstructs.2020.103141.

[33] R.J.A.M. Stevens, L.A. Martínez-Tossas, C. Meneveau, Comparison of wind farm large eddy simulations using actuator disk and actuator line models with wind tunnel experiments, Renew. Energy 116 (2018) 470–478, https://doi.org/10.1016/j.renene.2017.08.072.

[34] R. Corniglion, J. Harris, C. Peyrard, M. Capaldo, Comparison of the free vortex wake and actuator line methods to study the loads of a wind turbine in imposed surge motion, J. Phys. Conf. Ser. 1618 (2020), 052045, https://doi.org/10.1088/1742-6596/1618/5/052045.

[35] A. Arabgolarcheh, S. Jannesarahmadi, E. Benini, L. Menegozzo, Numerical study of a horizontal wind turbine under yaw conditions, Math. Probl Eng. 2021 (2021) 1–17, https://doi.org/10.1155/2021/9978134.

[36] A.S. Wise, E.E. Bachynski, Wake meandering effects on floating wind turbines, Wind Energy 23 (2020) 1266–1285, https://doi.org/10.1002/we.2485.

[37] L. Zhang, Y. Li, W. Xu, Z. Gao, L. Fang, R. Li, B. Ding, B. Zhao, J. Leng, F. He, Systematic analysis of performance and cost of two floating offshore wind turbines with significant interactions, Appl. Energy 321 (2022), 119341, https://doi.org/10.1016/j.apenergy.2022.119341.

[38] F. Porté-Agel, M. Bastankhah, S. Shamsoddin, Wind-turbine and wind-farm flows: a review, Boundary-Layer Meteorol. 174 (2020) 1–59, https://doi.org/10.1007/s10546-019-00473-0.

[39] H.M. Johlas, L.A. Martínez-Tossas, M.J. Churchfield, M.A. Lackner, D.P. Schmidt, Floating platform effects on power generation in spar and semisubmersible wind turbines, Wind Energy 24 (2021) 901–916, https://doi.org/10.1002/WE.2608.

[40] P. Cheng, Y. Huang, D. Wan, A numerical model for fully coupled aero-hydrodynamic analysis of floating offshore wind turbine, Ocean Eng. 173 (2019) 183–196, https://doi.org/10.1016/j.oceaneng.2018.12.021.

[41] Y. Huang, P. Cheng, D. Wan, Numerical analysis of a floating offshore wind turbine by coupled aero-hydrodynamic simulation, J. Mar. Sci. Appl. 18 (2019) 82–92, https://doi.org/10.1007/s11804-019-00084-8.

[42] H.G. Weller, G. Tabor, H. Jasak, C. Fureby, A tensorial approach to computational continuum mechanics using object-oriented techniques, Comput. Phys. 12 (1998) 620, https://doi.org/10.1063/1.168744.

[43] W.Z. Shen, W.J. Zhu, J.N. Sørensen, Actuator line/Navier-Stokes computations for the Mexico rotor: comparison with detailed measurements, Wind Energy 15 (2012) 811–825, https://doi.org/10.1002/we.510.

[44] W.Z. Shen, R. Mikkelsen, J.N.N. Sørensen, C. Bak, Tip loss corrections for wind turbine computations, Wind Energy 8 (2005) 457–475, https://doi.org/10.1002/we.153.

[45] W.Z. Shen, W.J. Zhu, J.N. Sørensen, Study of tip loss corrections using CFD rotor computations, J. Phys. Conf. Ser. 555 (2014), 012094, https://doi.org/10.1088/1742-6596/555/1/012094.

[46] A. Wimshurst, R.H.J. Willden, Analysis of a tip correction factor for horizontal axis turbines, Wind Energy 20 (2017) 1515–1528, https://doi.org/10.1002/we.2106.

[47] Z. Yu, X. Zheng, Q. Ma, Study on actuator line modeling of two NREL 5-MW wind turbine wakes, Appl. Sci. 8 (2018) 434, https://doi.org/10.3390/app8030434.

[48] M.H. Baba-Ahmadi, P. Dong, Validation of the actuator line method for simulating flow through a horizontal axis tidal stream turbine by comparison with measurements, Renew. Energy 113 (2017) 420–427, https://doi.org/10.1016/j.renene.2017.05.060.

[49] G. Deskos, M.D. Piggott, Mesh-adaptive simulations of horizontal-axis turbine arrays using the actuator line method, Wind Energy 21 (2018) 1266–1281, https://doi.org/10.1002/WE.2253.

[50] F. Papi, P.F. Melani, S. Xie, C. Perrone, P. Scienza, F. Balduzzi, A. Bianchini, Development and validation of an advanced actuator line model for wind turbines, E3S Web Conf. 312 (2021), 08004, https://doi.org/10.1051/E3SCONF/202131208004.

[51] J.N. So/rensen, W.Z. Shen, Numerical modeling of wind turbine wakes, J. Fluid Eng. 124 (2002) 393, https://doi.org/10.1115/1.1471361.

[52] X. Kong, L. Ma, C. Wang, S. Guo, M.A. Abdelbaky, X. Liu, K.Y. Lee, Large-scale wind farm control using distributed economic model predictive scheme, Renew. Energy 181 (2022) 581–591, https://doi.org/10.1016/J.RENENE.2021.09.048.

[53] M.A. Abdelbaky, X. Liu, D. Jiang, Design and implementation of partial offline fuzzy model-predictive pitch controller for large-scale wind-turbines, Renew. Energy 145 (2020) 981–996, https://doi.org/10.1016/J.RENENE.2019.05.074.

[54] J.M. Jonkman, M.L.J. Buhl, FAST user's guide - updated august 2005, Golden, CO, https://doi.org/10.2172/15020796, 2005.

[55] R. Chow, C.P. Van Dam, Verification of computational simulations of the NREL 5 MW rotor with a focus on inboard flow separation, Wind Energy 15 (2012) 967–981, https://doi.org/10.1002/WE.529.

[56] Y. Liu, Q. Xiao, A. Incecik, C. Peyrard, Aeroelastic analysis of a floating offshore wind turbine in platform-induced surge motion using a fully coupled CFD-MBD method, Wind Energy 22 (2019) 1–20, https://doi.org/10.1002/WE.2265.

[57] C.H.K. Wu, V.T. Nguyen, Aerodynamic simulations of offshore floating wind turbine in platform-induced pitching motion, Wind Energy 20 (2017) 835–858, https://doi.org/10.1002/WE.2066.

[58] N.N. Sørensen, J. Johansen, UPWIND, aerodynamics and aero-elasticity rotor aerodynamics in atmospheric shear flow, Eur. Wind Energy Conf. Exhib. 2007 2 (2007) 1233–1241. EWEC 2007.

[59] H. Lee, D.J. Lee, Effects of platform motions on aerodynamic performance and unsteady wake evolution of a floating offshore wind turbine, Renew. Energy 143 (2019) 9–23, https://doi.org/10.1016/j.renene.2019.04.134.

[60] B.D. Hirth, J.L. Schroeder, Documenting wind speed and power deficits behind a utility-scale wind turbine, J. Appl. Meteorol. Climatol. 52 (2013) 39–46, https://doi.org/10.1175/JAMC-D-12-0145.1.

[61] J. Wu, J.H. Ding, Y.P. He, Y.S. Zhao, Study on unsteady aerodynamic performance of floating offshore wind turbine by CFD method, Proc. Int. Offshore Polar Eng. Conf. (2015) 554–560, 2015-Janua.

[62] N. Sedaghatizadeh, M. Arjomandi, R. Kelso, B. Cazzolato, M.H. Ghayesh, Modelling of wind turbine wake using large eddy simulation, Renew. Energy 115 (2018) 1166–1176, https://doi.org/10.1016/j.renene.2017.09.017.

[63] S. Taghizadeh, F.D. Witherden, S.S. Girimaji, K. Hanjali, M. Tabib, A. Rasheed, T. Kvamsdal, LES and RANS simulation of onshore Bessaker wind farm: analysing terrain and wake effects on wind farm performance, J. Phys. Conf. Ser. 625 (2015), 012032, https://doi.org/10.1088/1742-6596/625/1/012032.

[64] J. Jonkman, Definition of the floating system for Phase IV of OC3. https://doi.org/10.2172/979456, 2010.

[65] D. Matha, Model development and loads analysis of an offshore wind turbine on a tension leg platform with a comparison to other floating turbine concepts: april 2009. https://doi.org/10.2172/973961, 2010.

[66] J.M. Jonkman, Dynamics Modeling and Loads Analysis of an Offshore Floating Wind Turbine, 2001.

[67] H. Lee, D.J. Lee, Numerical investigation of the aerodynamics and wake structures of horizontal axis wind turbines by using nonlinear vortex lattice method, Renew. Energy 132 (2019) 1121–1133, https://doi.org/10.1016/J.RENENE.2018.08.087.

[68] J. Dong, A. Viré, C.S. Ferreira, Z. Li, G. Van Bussel, A.C. Vire@tudelft, A.V. Nl, C. J. Simaoferreira@tudelft, C.S.F. Nl, G.J.W.V. Nl, A modified free wake vortex ring method for horizontal-Axis wind turbines, Energies 12 (2019) 3900, https://doi.org/10.3390/EN12203900, 12 (2019) 3900.

[69] T. Sebastian, M. Lackner, Analysis of the induction and wake evolution of an offshore floating wind turbine, Energies 5 (2012) 968–1000, https://doi.org/10.3390/EN5040968, 5 (2012) 968–1000.

[70] V.G. Kleine, L. Franceschini, B.S. Carmo, A. Hanifi, D.S. Henningson, Stability of floating wind turbine wakes, J. Phys. Conf. Ser. 1934 (2021), 012009, https://doi.org/10.1088/1742-6596/1934/1/012009.

[71] N. Ramos-García, S. Kontos, A. Pegalajar-Jurado, S. González Horcas, H. Bredmose, Investigation of the floating IEA Wind 15 MW RWT using vortex methods Part I: flow regimes and wake recovery, Wind Energy 25 (2022) 468–504, https://doi.org/10.1002/WE.2682.

[72] M. Bastankhah, F. Porté-Agel, Experimental and theoretical study of wind turbine wakes in yawed conditions, J. Fluid Mech. 806 (2016) 506–541, https://doi.org/10.1017/jfm.2016.595.

[73] O. Rand, A phenomenological modification for Glauert's classical induced velocity equation, J. Am. Helicopter Soc. 51 (2006) 279–282, https://doi.org/10.4050/1.3092889.

[74] Z. Gao, Y. Li, T. Wang, W. Shen, X. Zheng, S. Pröbsting, D. Li, R. Li, Modelling the nacelle wake of a horizontal-axis wind turbine under different yaw conditions, Renew. Energy 172 (2021) 263–275, https://doi.org/10.1016/J.RENENE.2021.02.140.

[75] R. Peraro, L. Menegozzo, A. Dal Monte, E. Benini, in: Extensive Validation of HAWT Unsteady Modelling Using BEM and CFD, vol. 12, Wind Energy, American Society of Mechanical Engineers, 2020, https://doi.org/10.1115/GT2020-16327.